Understanding the Spatial-Temporal Characteristics of Land Subsidence in Shenzhen under Rapid Urbanization Based on MT-InSAR

Min Sun, Yanan Du, Qingyao Liu, Guangcai Feng, Xing Peng, and Chunhua Liao

***Abstract*—Land subsidence is a common geological hazard in urban areas. It can be caused by human activities such as land reclamation and subway construction. However, rapid urbanization can accelerate the progress of these activities. Therefore, spatial-temporal analysis of land subsidence can provide a guarantee for rapid urbanization progress. In this study, Shenzhen, one of the fastest urbanizing cities in China, is selected for continued land subsidence monitoring. We collected 153 Sentinel-1A images from December 2015 to July 2021 and utilized an interferometric point target analysis method to generate the land subsidence in Shenzhen. Additionally, we analyzed the relationship between land subsidence and typical urbanization progress: land reclamation, transportation network, and urban construction. The results show that land subsidence mostly occurs in the western reclamation area, with a maximum rate of −74.9 mm/a in Qianhai Bay. Areas with larger quaternary marine sediment thickness in the range of 10–20 m are more likely to experience subsidence. Obvious subsidence (<−20 mm/a) along the subway mainly occurred on Lines 11 and Line 5, which is inversely proportional to the distance from the metro. The correlation coefficient is −0.197. Areas with low road densities have a high probability of experiencing great subsidence. A relationship between land subsidence and building construction in the Guangming district is found. Obvious subsidence (<−20 mm/a) mainly occurred in the building areas, with a percentage of 43.48%.**

***Index Terms*—Correlation analysis, IPTA-SBAS, land subsidence, urbanization.**

I. Introduction

LAND subsidence has become a worldwide threat to the safety of urban development. As one of the countries most affected by land subsidence, China is experiencing geological hazards in 17 provinces, affecting an area of 70 000 km^2 [1], [2]. However, the current situation of land subsidence in China deteriorates with urbanization progress, especially in cities with rapid urbanization. Additionally, in addition to land subsidence, other secondary disasters, such as sinkholes [3], urban flooding [4], infrastructure damage [5], and seawater intrusion in coastal areas [6], [7] can threaten people's lives and the normal operation of cities. Specific to the city of Shenzhen, it has undergone tremendous urbanization with the rapid development of the Guangdong–Hong Kong–Macao Greater Bay Area (GBA) in the past few decades [8]. Therefore, long-term monitoring of land subsidence and analysis of the relationship between land subsidence and urbanization are of great significance to the healthy development of cities.

Multitemporal InSAR (MT-InSAR) is a commonly used method for deformation monitoring that was developed from D-InSAR technology after overcoming the limitations caused by temporal-spatial decorrelation and atmospheric effects. It has been widely used in the fields of deformation monitoring for infrastructure [9], [10], [11], [12], mining [13], [14], landslides [15], [16], urban areas [17], [18], [19], earthquakes [20], [21], and volcanoes [22], [23], [24]. Among these applications, land subsidence under urbanization has been studied extensively. These studies mainly involved in spatial and temporal characteristics of ground deformation, cause analysis of land subsidence, and relationship exploration between land subsidence and building properties in the progress of urbanization. For example, the ground deformation monitoring under the project of "Mountain Excavation and City Construction" (MECC) in the Yan'an New District (YND) [25], [26], [27], [28]. Investigate the temporal and spatial patterns of land subsidence in Lanzhou New District and Ho Chi Minh City as a result of land reclamation and urban expansion [29], [30], [31], [32]. To generate the connection between the ground load and land subsidence, Chen et al. [33] and Zhou et al. [34] used the building IBI index and machine learning techniques to analyze the relationship between land subsidence and causes, such as static and dynamic load, groundwater level, and sediment thickness. In addition, other factors, including groundwater extraction, building construction, geological strata difference, and seasonal precipitation can also contribute to urban land subsidence [35], [36], [37], [38]. In Pisa, Italy, Solari et al. studied the connection between land subsidence and the age of buildings [39]. Yang et al. showed a weak correlation between

Manuscript received 10 November 2022; revised 23 January 2023 and 28 February 2023; accepted 29 March 2023. Date of publication 5 April 2023; date of current version 8 May 2023. This work was supported in part by the Science and Technology Projects in Guangzhou under Grant 2023A04J1542, in part by the National Natural Science Foundation of China under Grant 41804003, in part by the Graduate Innovation Research Funding Program of Guangzhou University under Grant 2021GDJC-M21. *(Corresponding author: Yanan Du.)*

Min Sun, Yanan Du, Qingyao Liu, and Chunhua Liao are with the Center of GeoInformatics for Public Security, School of Geography and Remote Sensing, Guangzhou University, Guangzhou 510006, China (e-mail: 2112001074@e.gzhu.edu.cn; yndu@gzhu.edu.cn; 2112001068@e.gzhu.edu.cn; 2001400024@e.gzhu.edu.cn).

Guangcai Feng is with the School of Geosciences and Info-Physics, Central South University, Changsha 410083, China (e-mail: fredgps@csu.edu.cn).

Xing Peng is with the School of Geography and Information Engineering, China University of Geosciences, Wuhan 430073, China (e-mail: pengxing@cug.edu.cn).

This article has supplementary downloadable material available at https://doi.org/10.1109/JSTARS.2023.3264652, provided by the authors.

Digital Object Identifier 10.1109/JSTARS.2023.3264652

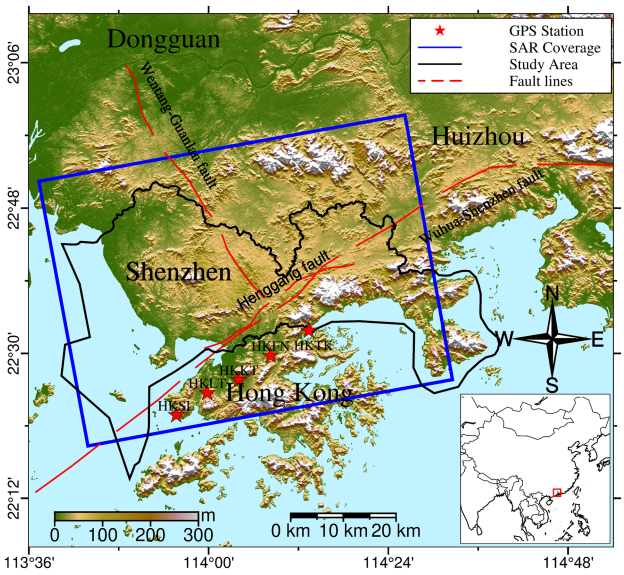

Fig. 1. Study area and data coverage. The blue rectangle represents the coverage of the Sentinel-1A dataset. The red dotted lines denote the surrounding faults. The red stars show the locations of the GPS stations in Hong Kong. The black solid line is the study area of Shenzhen.

ground subsidence and building volume in the Chaoyang and Tongzhou districts of Beijing [40].

In the case of Shenzhen, the hot spots of research are land reclamation and underground space excavation. For example, Xu et al. confirmed a strong connection between land reclamation and subsidence in the coastal area of Shenzhen [41], [42]. Additionally, subway construction is a factor that can contribute to land subsidence, according to Hu et al. [43] and Liu et al. [44]. He et al. employed InSAR and LiDAR data to study the connection between ground subsidence and buildings in Shenzhen [45]. The findings revealed that subsidence was primarily brought on by new buildings. However, few studies have linked surface subsidence to urbanization characteristics in Shenzhen thus far. Therefore, three typical urbanization processes, land reclamation, transportation network including subway network and ground road network, and urban construction were adopted to analyze the relationship between urbanization and land subsidence. The findings of this work can provide valuable information for urban planning and key points of potential geologic hazard monitoring of similar cities.

In this study, we calculated the time series deformation of Shenzhen in the last six years based on the IPTA-SBAS method. Then, we analyzed the characteristics of subsidence with external datasets, such as optical images, geological data, and road data. We generated the relationship between land subsidence and urbanization with GIS spatial analysis and a correlation index.

II. Study Area, Datasets, and Method

A. Regional Overview

Shenzhen, one of the largest cities in China, is located in the south of Guangdong Province (22° 26′–22° 51′ N, 113° 45′ - 114° 37′ E). As shown in Fig. 1, the entire city has a high northeast and low southwest topography. In the south and west of the city, it is surrounded by the ocean with an elevation between 1–10 m, but the average elevation in the northeast reaches 80 m because it is covered by mountains there. The geological structure of Shenzhen is complex, and the fracture structure is the main component of the city. There are three primary faults crossing the city: the Henggang fault, the Wentang-Guanlan fault, and the Wuhua-Shenzhen fault [46].

In terms of urban development, Shenzhen is one of the Special Economic Zones (SEZ) in China after the reform and opening-up policy. It has experienced a series of urbanization processes since 1980. We selected three typical processes, land reclamation, development of transportation networks, and urban construction, to analyze the evolution of urbanization in Shenzhen. Land reclamation is one of the important methods used to expand the area of the city and accelerate urbanization. According to the statistics, Shenzhen's reclaimed land area exceeds 74.77 km^2, and it will continue to increase in accordance with the Five-Year Action Plan for Urban Infrastructure Construction in Shenzhen (2021–2025). Another aspect of urbanization is the construction of the subway network. Currently, 11 subway lines have been completed and put into use. By 2025, another five subway lines will be planned, and the accumulated subway miles will reach 647 kilometers. As for urban construction, a mass of mountains has been excavated to build infrastructure in Guangming and Longgang districts in recent years, especially when the policy "Several Opinions on Supporting Guangming Science City to Build a World-class Science City" was proposed in 2019. Besides, to get a clear understanding of the urbanization process in Shenzhen, we also collected the landmark events of each typical urbanization process, as shown in Table S1.

B. Datasets

We collected 153 Sentinel-1A images from December 2015 to July 2021 to obtain the time series deformation of Shenzhen. These SAR images are retrieved from ASF DAAC, and processed by ESA. The orbit number is 40 858 and the number of two adjacent frames is 65 and 71. The coverage of these images is shown in Fig. 1. The 1-arc Shuttle Radar Topography Mission (SRTM) is used as an external DEM. We also collected datasets from five GPS stations located in Hong Kong to evaluate the accuracy of the InSAR results. Additionally, we also collected some geological datasets [47], historical optical images (from Google Earth), and road network data of Shenzhen (https://www.ritu.cn/) to analyze the relationship between land subsidence and urbanization.

C. IPTA-SBAS Method

Interferometric point target analysis (IPTA) is a commonly used MT-InSAR method to generate time series deformation. Different from the traditional MT-InSAR methods, such as SBAS-InSAR [48] and PS-InSAR [49], IPTA-SBAS adopts an iterative method to refine the coherence points and estimate the parameters simultaneously. First, the IPTA-SBAS method generates interferometric pairs with temporal and perpendicular baseline thresholds. The differential interferograms are obtained

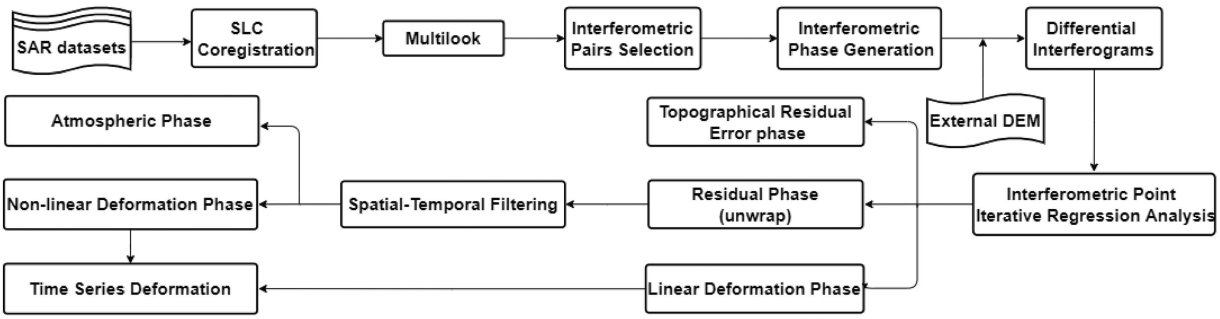

Fig. 2. Workflow of IPTA-SBAS.

with standard D-InSAR procedures [50]. Second, an iterative regression analysis is utilized to compute the residual topography. For each iteration, the residual phase is unwrapped with an MCF method, and the coherent candidates are refined with a given threshold for the residual phase. Then, linear deformation is calculated based on the unwrapped phase after removing the residual topographic phase. Finally, the nonlinear deformation is separated from the atmospheric signal with a spatial-temporal filtering procedure. The final time series deformation is generated by adding the nonlinear deformation and the linear deformation. Fig. 2 illustrates the flowchart of IPTA-SBAS.

Specifically, IPTA-SBAS is executed in the following three steps.

Step 1: Differential interferometric phase generation. In this study, 2017 119 was chosen as the master image, and slave images were coregistered to the master image. A total of 446 interferometric pairs were selected with temporal and perpendicular baseline thresholds of 100 days and 150 m, respectively. The topographical phase was removed with the 1-arc SRTM DEM. A multilook operation, 8 and 2 in the range and azimuth directions, respectively, was adopted to reduce phase noise.

Step 2: Iterative regression analysis. The residual topographical error phase was estimated by three separated parts. The first part, denoted as ΔZ_1, was calculated by 1-D regression analysis. The unknown parameter is the residual topographic phase, and the observation is the original wrapped differential phase. A threshold of residual phase, 1.3 rad in this study, was adopted to improve the accuracy of the parameter and refine the coherence candidates [51]. Additionally, the wrapped residual phase was unwrapped with the MCF method, and part of the atmospheric phase was estimated by spatial filtering. The window size of the filtering is set as 1600 m empirically. The second part, denoted as ΔZ_2, was estimated with the abovementioned iterative 1-D regression analysis. However, the observation is the remaining phase after subtracting the partial atmospheric phase and residual topographic phase from the unwrapped phase. The third part, denoted as ΔZ_3, was calculated by the 2-D regression analysis method. The unknown parameters are the third part of the residual topographical phase and the linear deformation rate.

Step 3: Separation between nonlinear deformation and atmospheric signals. The atmospheric signal was estimated by high-pass temporal filtering following low-pass spatial filtering. The windows for temporal and spatial filtering are 180 days and 800 m [52], respectively. Nonlinear deformation was generated after removing the atmospheric phase from the residual unwrapped phase. The final time series deformation was the sum of the linear deformation and nonlinear deformation.

III. Results and Analysis

The average deformation rate of Shenzhen was calculated by the IPTA-SBAS, as shown in Fig. 3. Considering the weak horizontal deformation in Shenzhen [41], we used the deformation in the line-of-sight (LOS) direction to analyze the spatial-temporal characteristics in the following sections. Positive value represents movement toward the satellite (uplift), while negative value represents movement away from the satellite (subsidence). The deformation magnitude of the inland is gentle, ranging from −15 mm/a to 5 mm/a. The subsidence is mainly distributed along the coastal areas with a maximum rate of 74.9 mm/a. Compared with the eastern area of the city, obvious subsidence is mainly distributed on the western coastline area.

A. Characteristics of Subsidence in the Land Reclamation Area

Land reclamation is a significant urbanization symbol in Shenzhen. As shown in Fig. 3(a), the changes in the coastline between 1979 and 2021 represent the land reclamation area, where land subsidence is mainly concentrated. To analyze the characteristics of subsidence, five areas with subsidence rates over 15 mm/a were selected, as shown in Fig. 3(b)–(f).

Area S1 is located in the northwestern part of Shenzhen. The subsidence in this area is mainly distributed in the land reclamation area (zone 1) and on both sides of the Dongbao River (D.R) (zone 2), as shown in Fig. 3(b). The largest settlement occurred in the Shenzhen Convention and Exhibition Center (zone 3), with a maximum subsidence rate of 42.0 mm/a. Area S2 is located around Baoan International Airport (B.I.A), with three obvious subsidence zones [zones 1–3 in Fig. 3(c)]. Zone 1 and Zone 2 are within Baoan International Airport, whose maximum subsidence rates reach 39.8 mm/a and 23.3 mm/a, respectively. Zone 3 is located outside the airport with a maximum rate of 66.2 mm/a.

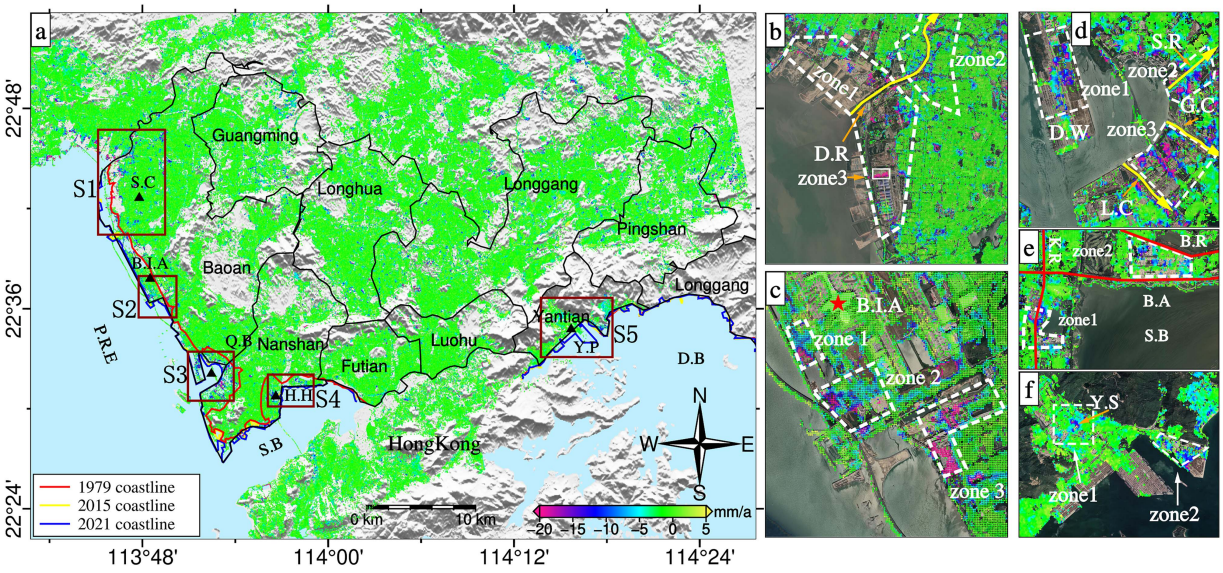

- P.R.E:Pearl River Estuary
- S.C:Shajing Community
- Y.P:Yantian Port
- D.W:Dachanwan Wharf
- L.C:Liantong Canal
- B.R:Baishi Road
- B.I.A:Baoan International Airport
- H.H:Houhai
- D.B:Dapeng Bay
- S.R:Shuangjie River
- K.R:Keyuan Road
- Y.S:Yantianlu Station
- Q.B:Qianhai Bay
- S.B:Shenzhen Bay
- D.R:Dongbao River
- G.C:Guimiao Canal
- B.A:Binhai Avenue

Fig. 3. (a) Average deformation rate of Shenzhen from December 2015 to July 2021. The red, yellow, and blue lines represent the coastline of Shenzhen in 1979, 2015, and 2021, respectively. The red rectangles represent areas with obvious subsidence. The black polygons represent the boundary of each district of Shenzhen. (b)–(f) The enlarged views of areas S1–S5 in (a). The white dotted polygons represent the primary subsidence area. The yellow arrows indicate the flow direction of rivers, the red star represents the Baoan International airport, and the red solid lines indicate the primary road in area S4.

In Nanshan District, subsidence is mainly located in Qianhai Bay (Q.B) and Houhai (H.H), marked as area S3 and area S4 in Fig. 3(a). Subsidence in Qianhai Bay is concentrated in three zones, as shown in Fig. 3(d). Zone 1 is located at Dachanwan wharf (D.W), and Zone 2 and Zone 3 are located between the Liantong canal (L.C) and Shuangjie River (S.R). The maximum subsidence rates are 38.2 mm/a, 29.8 mm/a, and 35.2 mm/a, respectively. Unlike the case in Qianhai Bay, subsidence in Houhai Bay is mainly located along the roads, as shown in Fig. 3(e). The maximum subsidence rates of Zone 1 and Zone 2 are 44.3 mm/a and 28.7 mm/a, respectively.

Area S5 is situated in Yantian Port (Y.P), one of the major ports in Shenzhen. Two obvious subsidence zones are identified, as shown in Fig. 3(f). Zone 1 is near the Yantianlu subway station (Y.S), with a maximum settlement rate of 22.1 mm/a. Zone 2 is within the land reclamation area, and the maximum subsidence rate is approximately 17.8 mm/a. Compared with the other four areas, the subsidence in Area S5 is the smallest.

B. Accuracy Verification

We collected five GPS stations (HKTK, HKSL, HKLT, HKKT, and HKFN) derived from the Nevada Geodetic Laboratory (NGL) to verify the results of IPTA-SBAS [53]. GNSS datasets derived from the NGL are usually used as the true value of surface deformation [54], [55]. The GPS results have been translated to the line of sight (LOS) direction of SAR images according to the equations described in [6]. Then, the relative values of InSAR were calibrated to the absolute values according to the reference HKTK station. For each GPS station, InSAR measurement points located within a circle with a radius of 100 m are selected to calculate the mean deformation value, which is a proxy for the comparison with two measurements, as shown in Fig. 4 [56]. The root mean square error (RMSE) between the two results for the four stations is 6.9 mm, 8.0 mm, 6.5 mm, and 6.8 mm, which evaluates the accuracy of the IPTA-SBAS results.

C. Characteristics of Subsidence Along the Subway Line

Underground exploitation, especially the construction and operation of subways, is a common method for urban traffic expansion and a symbol of the urbanization process. However, overexploitation in urban areas may lead to geological hazards such as land subsidence and sinkholes [57], [58]. In this study, 11 subway lines with a 500 m buffer zone of Shenzhen are analyzed, and the deformation results are shown in Fig. 5. We assumed that subsidence with a rate over 10 mm/a was mainly caused by subway tunneling. Four representative areas with subsidence rates exceeding 20 mm/a were identified; see the enlarged views in Fig. 5. The maximum subsidence rates of area S1 to area S4 are 34 mm/a, 66.2 mm/a, 35.5 mm/a. and

TABLE I
STATISTICAL RESULTS OF LAND SUBSIDENCE ALONG THE SUBWAY LINE

Subway Lines	Coherent points number	Maximum subsidence rate (mm/a)	Coherent points percentage (>10 mm/a)	Location	Start time of operation (yyyy-mm-dd)/Operation time (year)
Line 11	39541	71.5	3.2%	coastal	2016-06-28/5.08
Line 5	35220	53.5	2.6%	inland	2011-06-22/10.1
Line 1	35249	33.9	1.2%	coastal	2004-12-28/16.58
Line 8	6612	22.1	1.1%	coastal	2020-10-28/0.74
Line 10	22390	40.5	1%	inland	2020-08-18/0.93
Line 9	22725	23.5	1%	coastal	2016-10-28/4.74
Line 6	36486	28.6	0.8%	inland	2020-08-18/0.93
Line 2	31749	47.3	0.6%	coastal	2010-12-28/10.58
Line 4	24928	27.5	0.5%	inland	2004-12-28/16.58
Line 7	24793	24.1	0.2%	inland	2016-10-28/4.74
Line 3	39130	23.7	0.2%	inland	2010-12-28/10.58

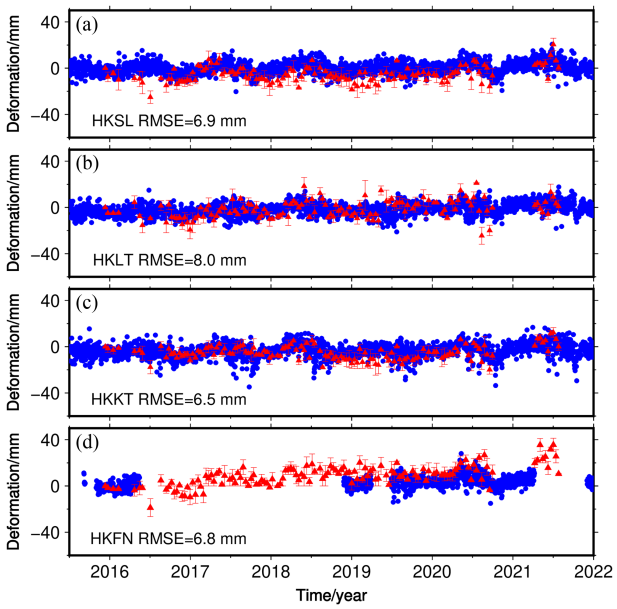

Fig. 4. Verification of the IPTA-SBAS result. The blue dotted circles and red triangles represent the time series deformation of GPS and IPTA-SBAS, respectively.

20.8 mm/a, respectively. Three of the four areas (S2, S3, and S4) are distributed along the coastal area, which is consistent with the overall regional subsidence characteristics. In addition, the area with the largest subsidence is located at Line 11, with a maximum subsidence rate of 71.5 mm/a.

To further analyze the subsidence characteristics of the subway lines, we counted the number of coherent points, the maximum subsidence rate, the percentage of coherent points with a subsidence rate greater than 10 mm/a, the location, the completion time, and the operation time of each line. We ranked the 11 subway lines in descending order of the coherent point percentage, as shown in Table I. Four subway lines with maximum subsidence rates exceeding 40 mm/a, that is, Lines 2, Line 5, Line 10, and Line 11. The corresponding maximum rates of the four lines are 47.3 mm/a, 53.5 mm/a, 40.5 mm/a, and 71.5 mm/a, respectively. Additionally, the top two subway lines in the coherent point percentage are Line 5 and Line 11, with values of 2.6% and 3.2%, respectively. Line 11 is located along the coastal area, while Line 5 is located inland. Considering the subsidence and location of the subway lines, we selected Line 5 and Line 11 for a more comprehensive analysis.

The subsidence along Line 5 is concentrated in two zones: one is located in Qianhai Bay, while the other is located between Shenzhen North station and Shangshuijing station, as shown in the enlarged view of Fig. 6(a). In Zone 1, we detected four areas with obvious subsidence funnels to analyze the subsidence features along the subway [see Fig. 6(b)–(e)]. In Fig. 6(b), (d), (e)), the subsidence funnels are close to the subway station, and the maximum subsidence rate of each bowl was quite similar, approximating 16 mm/a, 15.2 mm/a, and 17.5 mm/a, respectively. In Fig. 6(c), the subsidence was located in a parking lot near the Pearl River Delta Ring Expressway with a maximum subsidence rate of 29.4 mm/a. The average deformation rate of this subsidence bowl is over 20 mm/a, which is the most serious among the four funnels. It is noted that the subsidence in Qianhai Bay (Zone 2) will be analyzed in the following section due to the overlap between Line 5 and Line 11.

Line 11 was constructed from April 2012 and was put into operation in June 2016. Different from the centralized subsidence of Line 5, the subsidence distribution of Line 11 is dispersed. Five areas with subsidence rates greater than 20 mm/a were observed near Songgang station (area S1), Houting station (area S2), Jinwan Avenue (area S3), Qianhaiwan station (area S4), Hongshuwannan station, and Shenwan station (area S5), as shown in Fig. 7(a). In areas S1, S2, S4, and S5, subsidence was mainly gathered around subway stations, and the maximum subsidence rates of the four areas are 33.2 mm/a, 22.9 mm/a, 34.0 mm/a, and 20 mm/a, respectively. In addition to the subsidence near the subway station, another subsidence funnel within area S3 is distributed along Line 11. The subsidence funnel is located in an industrial park, with mean and maximum subsidence rates of 29.2 mm/a and 71.5 mm/a, respectively. Among these five areas, the subsidence in area S3 is the most severe, and the largest total subsidence area occurs in area S4. Moreover, fieldwork was carried out in area S3, which is located at the south of Baoan International Airport [point TP1 in Fig. 7(a)], as shown in Fig. 8. Obvious subsidence (approximate 8 cm) of the building was observed, which can also evaluate the reliability of InSAR results.

To analyze the temporal feature of subsidence along Line 11, we plotted the time series deformation of six typical points (P1-P6) in area S3 and area S4 by considering the magnitude

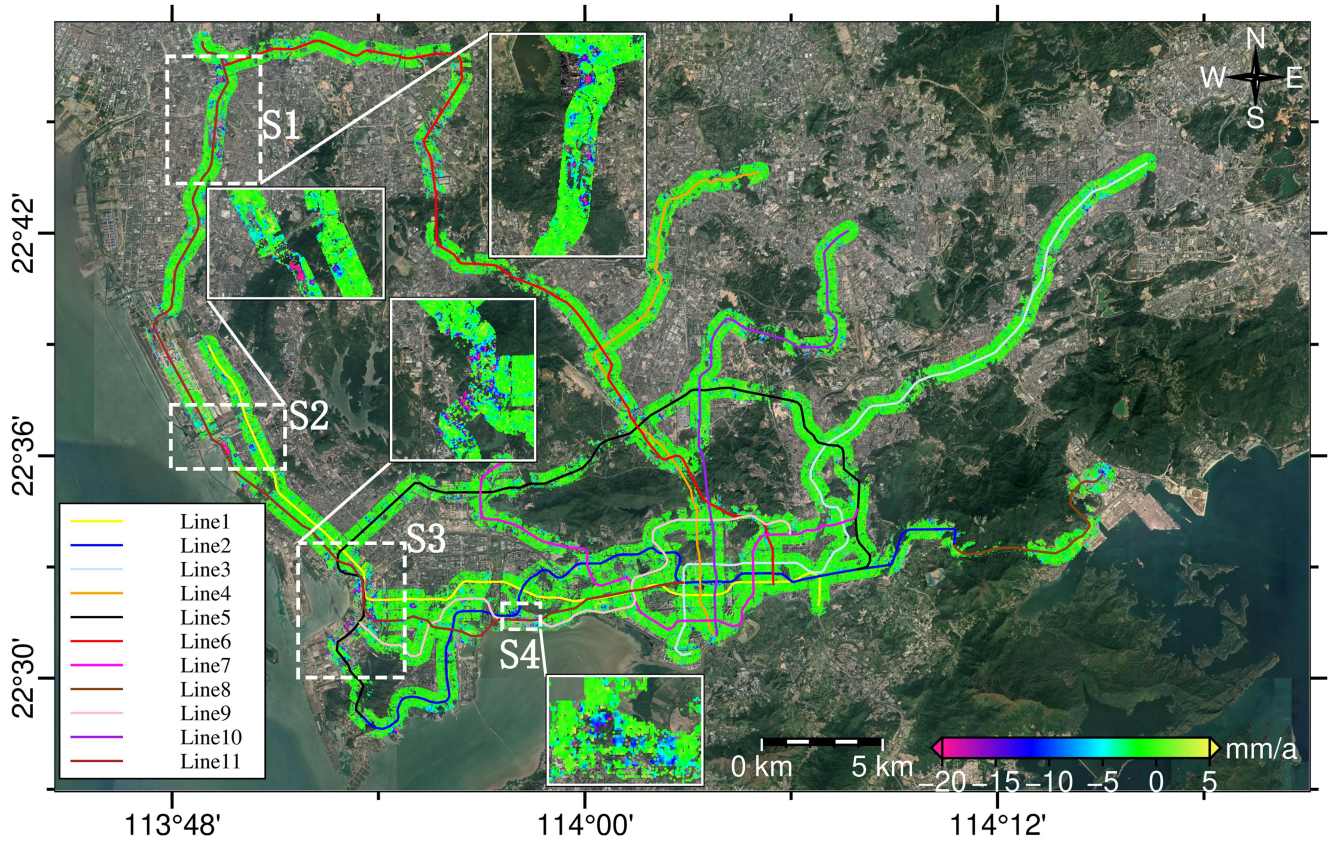

Fig. 5. Subsidence along the Shenzhen subway network. Solid lines with different colors represent 11 subway lines. The white dashed lines represent the selected areas with subsidence rates over 20 mm/a.

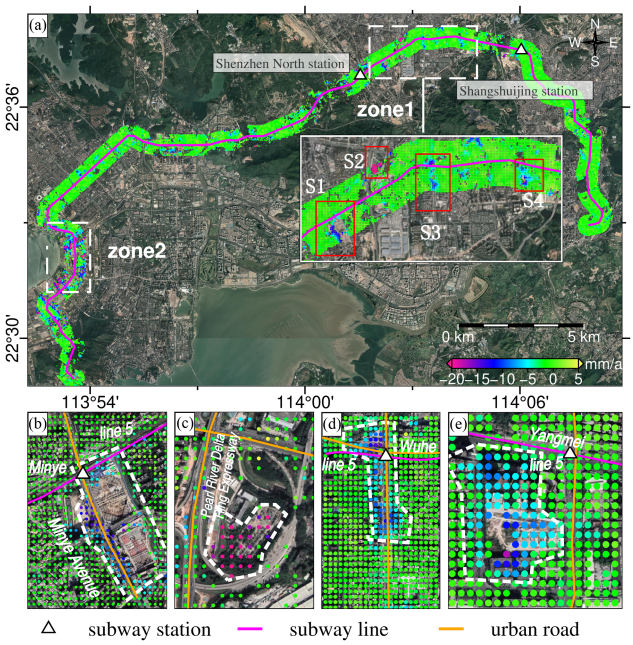

Fig. 6. (a) indicates the subsidence along subway Line 5. The dotted white rectangles represent two selected areas along the Line 5, named zone 1 and zone 2. The red rectangles represent four typical subsidence areas (S1–S4) in zone 1. The magenta solid line represents Line 5. (b)–(e) indicate the enlarged views of area S1–S4 in (a). The yellow solid lines represent the primary road around the subsidence area, and the white dashed polygons represent the boundary of the subsidence area. The white triangles represent the subway stations.

and area of subsidence. The deformation trend of P1-P3 in area S3 was nearly linear, as shown in Fig. 7(b), (d), (f). The distance from P1, P2, and P3 to Line 11 are 153 m, 248 m, and 349 m, respectively. The cumulative settlements of P1 and P2 are 16 cm and 8 cm, respectively, while the cumulative settlement of P3 was almost 0 cm, which is inversely proportional to the distance along the subway. Contrary to the characteristics of P1-P3 in area S3, the time series deformation of P4-P6 in area S4 shows an obvious periodic trend [see Fig. 7(c), (e), (g)]. The cumulative settlements of P4, P5, and P6 are 14.27 cm, 16.1 cm, and 3.6 cm, respectively. The reason for these two different deformation trends is probably caused by the intervention of human activities in the coastal land reclamation area; that is, the linear deformation in area S3 may be in the initial stage of soft soil compaction; however, the periodic deformation in area S4 probably related to the planned construction work around the commercial center of Qianhai Bay.

In addition, we calculated the correlation between the coherent point percentage and the operation time, as shown in Fig. S1. The result is −0.08, indicating that there is no obvious relationship between operation time and subsidence in the case of Shenzhen subway.

D. Characteristics of Subsidence in Guangming District

Guangming district was approved in 2018, and it is one of the newest districts of Shenzhen. As an important node of the

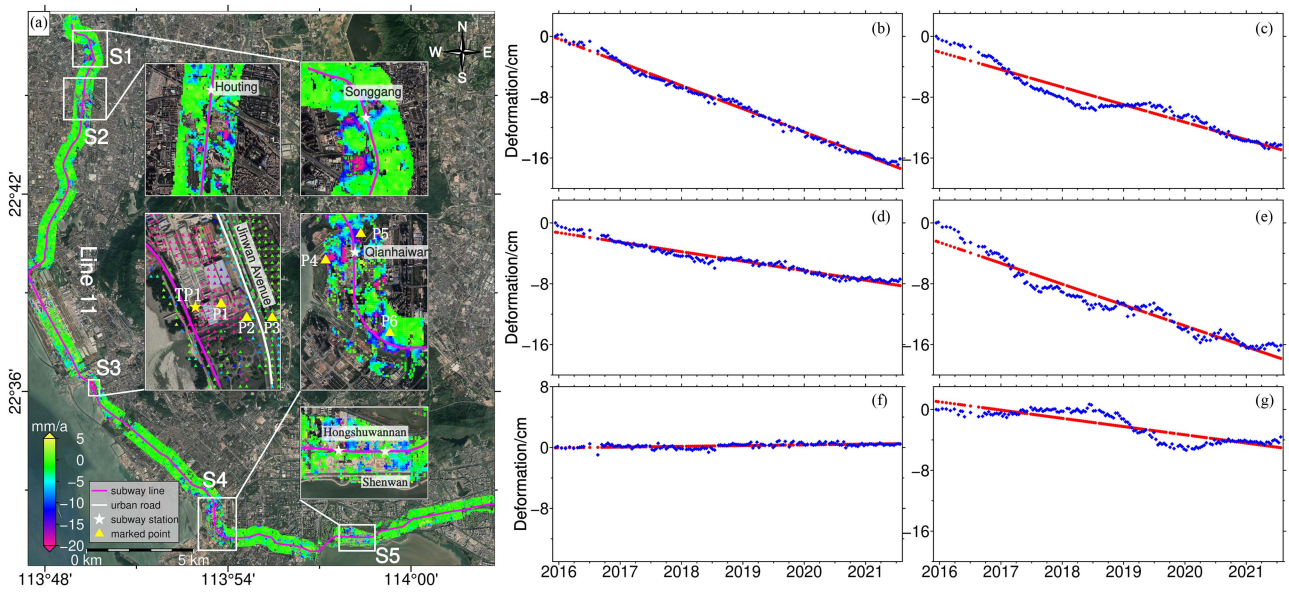

Fig. 7. (a) Subsidence along the subway Line 11. The purple line and the white line represent the subway line and the primary road, respectively. The white stars represent the subway stations. The yellow triangles represent the selected points P1-P6. The enlarged views represent the five selected areas (S1–S5) with obvious subsidence. (b)–(g) The time series deformation of P1-P6. The blue points are the cumulative deformation of the MT-InSAR and the red lines represent the linear fitting values of the deformation.

Fig. 8. Fieldwork in the south of Baoan International Airport.

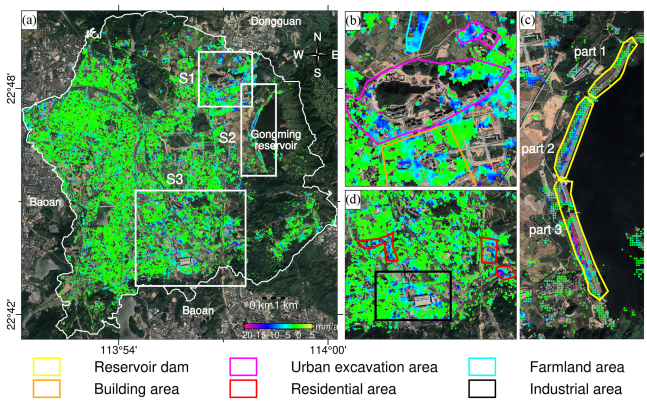

Fig. 9. (a) Land subsidence of the Guangming district. The white rectangles represent the selected subsidence area (S1–S3). (b)–(d) The enlarged views of area S1–S3 in (a). The yellow polygons represent the Gongming Reservoir dam. The purple polygons, cyan polygons, gray polygons, red polygons, and black polygons represent the urban excavation area, farmland area, building area, residential area, and industrial area, respectively.

Guangzhou–Shenzhen Science and Technology Corridor and an important area of the Guangdong–Hong Kong–Macao Bay Area (GBA), Guangming District has carried out much work to promote urbanization, such as infrastructure construction and land excavation, in the past few years. Therefore, we choose the Guangming district as a representative for the urbanization of Shenzhen. The deformation result of the Guangming district is shown in Fig. 9(a). The subsidence is mainly distributed in the south and northeast of the Guangming district. Three areas with obvious subsidence are selected to analyze the causes of the deformation, marked as S1, S2, and S3 in Fig. 9(a). In area S1, the subsidence is mainly located in the development zone that is derived from vegetation and agricultural land, as shown in Fig. 9(b). The subsidence is probably caused by the engineering construction. Unlike the situation in area S1, the subsidence in area S3 is mainly distributed in the industrial and residential areas, as shown in Fig. 9(d). The discrete subsidence is most likely caused by groundwater exploitation for industrial and domestic water. In area S2, the subsidence is mainly concentrated on the Gongming Reservoir, as shown in Fig. 9(c). To better understand the subsidence process of the reservoir, we divided the dam into three parts according to the chronological order of construction. As we expected, the subsidence is inversely proportional to the construction time; that is, Part 3 experiences the largest settlement, Part 2 follows, and Part 1 is the last. The cumulative settlement in Part 2 and Part 3 reached 8.2 cm and 23.6 cm, respectively.

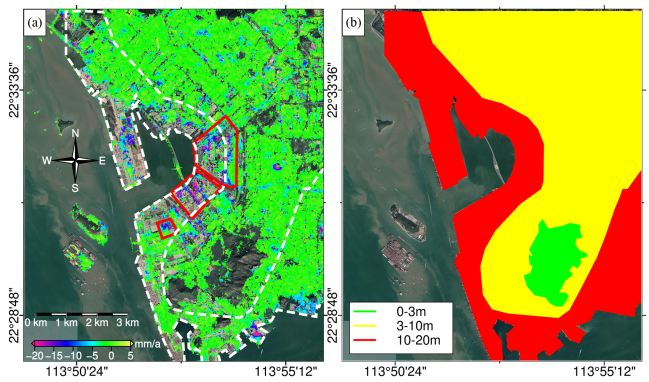

Fig. 10. (a) Land subsidence and (b) sediment thickness of Qianhai Bay. The red solid polygons represent areas of intense subsidence, and the white dotted polygons represent areas with sediment layer thicknesses over 10 m.

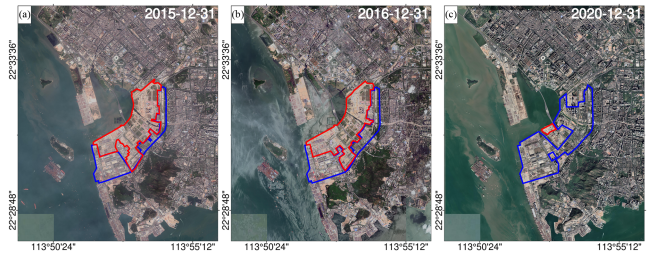

Fig. 11. Land use change in Qianhai Bay from December 2015 to December 2020. The red and blue polygons represent changes in the built-up area and the to-be-built-up area, respectively.

IV. Discussion

A. Causes of Land Subsidence in Qianhai Bay

Qianhai Bay is a typical reclamation area with obvious subsidence, as shown in Fig. 10(a), which is the future financial center of Shenzhen. The reclaimed land area exceeds 7.7 km^2. To understand the causes of subsidence, we collected sediment thickness data of Qianhai Bay, as shown in Fig. 10(b). The sedimentary layer has the characteristics of large porosity, high water content, and high compressibility. Ground with a thick sedimentary layer is more prone to deformation [59]. We found that subsidence is mainly situated in the zone, where the sediment thickness is between 10 and 20 m. Some discrete settlements were also found in areas with sediment thickness between 3 and 10 m. It is noted that areas with sediment thickness below 3 m are located in mountainous areas, Nanshan Park of Shenzhen, resulting in low point density of InSAR technique. Subsidence in this area is not obvious. The abovementioned features indicate that sediment thickness may be an important cause of subsidence in Qianhai Bay. In addition to the geological conditions, we also analyzed the infrastructure construction of Qianhai Bay due to its important economic position. We collected three optical images corresponding to the acquisition time of SAR images and generated the built-up areas of Qianhai Bay with visual interpretation. The results are shown in Fig. 11. The range of the changing built-up area is consistent with the location of subsidence, which indicates that urban construction may be one of the factors affecting land subsidence in this area [45].

TABLE II
Spearman's Correlation Coefficient Between Subsidence Rate and Distance Along the Subway

Grade	Correlation points subsidence rate interval (mm/a)	Spearman's correlation coefficient
1	20.5 to 49.5	-0.197
2	10.8 to 20.5	0.070
3	5.9 to 10.8	0.009
4	0 to 5.9	0.059

B. Relationship Between Land Subsidence and Subway

As described in Section III-C, obvious subsidence is observed along the subway. However, the relationship between land subsidence and subway distance is still unclear. To generate the relationship between these two factors, we adopted a proximity analysis to extract the minimum distance of each point from the subway. First, we set a distance threshold (500 m in this case) to select valid coherent points. Next, the distance from the subway was set as the independent variable, and the subsidence rate was set as the dependent variable. To better analyze the relationship, we divided the subsidence rate into four classes according to the natural breakpoint method. Then, the correlation between subsidence and subway distance was calculated based on Spearman's rank correlation coefficient method [33]. The results are shown in Table II. A negative correlation between the subsidence rate and distance from the subway is found when the subsidence rate is between 20.5 and 49.5 mm/a. The spearman's rank correlation coefficient is -0.1967. This indicates that regions closer to the subway may be more prone to land subsidence. But this correlation is quite weak [60], which means that the impact of distance from the subway on land subsidence is relatively small at present.

C. Relationship Between Land Subsidence and Road Network Density

In addition to the underground subways, Shenzhen also has abundant ground transportation. The mileage of the road network reached 7500 km in 2020, an increase of approximately 1000 km compared with 2015. To investigate the relationship between subsidence and the road network, we calculated the road network density of Shenzhen with a grid whose size was 1000 m $\times$ 1000 m. The road network density is defined as the road mileage of each grid divided by the grid area. It is noted that the road network density in this section represents the progress of urban exploitation. For example, higher road network density means less engineering construction. By contrast, lower road density means areas were under construction, which can also lead to land subsidence. Then, we divided the road network density grids into five levels according to the natural breakpoint method. Areas with higher road network density are mainly concentrated in southern and northeastern Shenzhen, as shown in Fig. 12. Similarly, we classified the subsidence rate into five classes and counted the corresponding coherent point percentage of each road network density level, as shown in Fig. 13(a). We noticed that the coherent point percentage has a negative

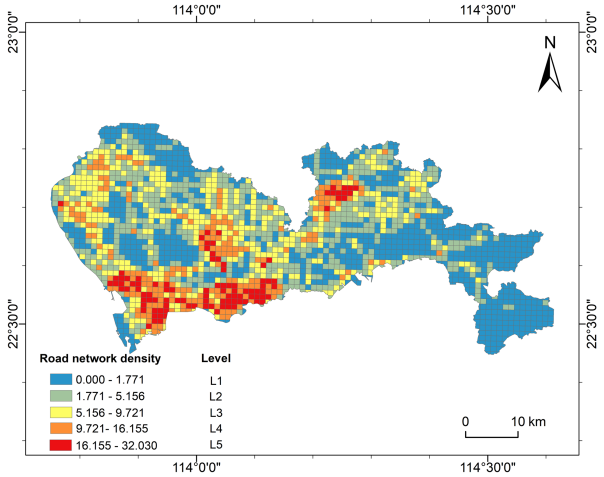

Fig. 12. Road network density of Shenzhen. The blue, green, yellow, orange, and red blocks represent the road network density of levels L1, L2, L3, L4, and L5, respectively.

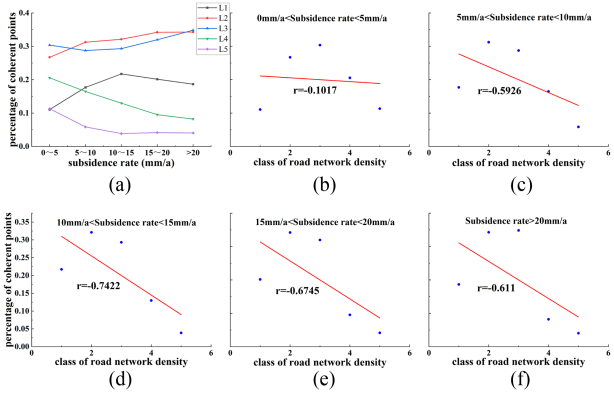

Fig. 13. (a) Relationship between the subsidence rate and the coherent point percentage. The black, red, blue, green, and purple lines represent the relationship for the road density of L1 to L5, respectively. (b)–(f) Relationship between road density classes and coherent point percentage. (b)–(f) are the corresponding results of subsidence rates ranging from 0–5 mm/a, 5–10 mm/a, 10–15 mm/a, 15–20 mm/a, and greater than 20 mm/a, respectively.

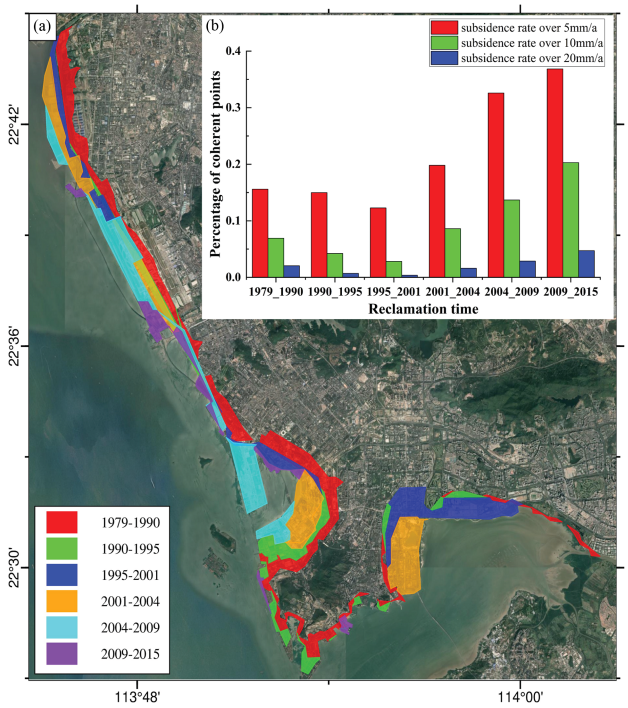

Fig. 14. (a) Land reclamation evolution in Shenzhen. The red, green, blue, orange, cyan, and purple blocks represent the reclamation area from 1979 to 1990, from 1990 to 1995, from 1995 to 2001, from 2001 to 2004, from 2004 to 2009, and from 2009 to 2015, respectively. (b) Histogram between reclamation time and percentage of coherent points. The red, green, and blue bars represent the results of points with subsidence rates over 5 mm/a, 10 mm/a, and 20 mm/a, respectively.

TABLE III
CORRELATION COEFFICIENT TEST BETWEEN SELECTED FACTORS AND LAND SUBSIDENCE IN RECLAMATION AREA

Factors	Distance from the coastline	Distance from the subway line	Road density
Correlation coefficient	–0.101	–0.084	–0.122

correlation with the subsidence rate when the road network density is higher (L4, L5). In contrast, a positive correlation between the coherent point percentage and subsidence rate is observed when the road network density is low (L1, L2, L3). Additionally, we also plot the scatter map between the road network density and the coherence point percentage for five subsidence rate classes, as shown in Fig. 13(b)–(f). We note that there is a negative correlation between the road network density level and coherent point percentage when the subsidence rate is over 5mm/a, as shown in Fig. 13(c)–(f). The above study indicates that areas with low road network density may be more likely to occur obvious subsidence, which can be caused by abundant engineering construction.

D. Evolution Feature of Land Subsidence in the Reclamation Area

Land reclamation is a typical symbol in Shenzhen's urbanization process, which can lead to land subsidence in different degrees. To analyze the evolution feature of land subsidence in reclamation areas, we obtained the changes in reclamation areas from 1979 to 2015 with the assistance of optical images derived from Google Earth. We first divided the reclamation time into six phases, as shown in Fig. 14(a). It is noted that the coastline is stable and there is no significant new reclamation area since 2015. Then, we calculated the percentage of coherent points with subsidence rates over 5, 10, and 20 mm/a in the partitioned reclamation areas. The results are shown in Fig. 14(b). Two different subsidence stages were found for the three subsidence rate intervals. The coherent point percentage of each subsidence rate interval became decreased with the accumulation of reclamation time from 1979 to 2001, which is consistent with the settlement law of landfill or reclamation areas: the subsidence rate slows down with time [61]. However, subsidence became active with the reclamation time since 2001, indicating that the subsidence in the reclamation area is probably in an increasing trend. It will take some time for the subsidence to stabilize. Moreover,

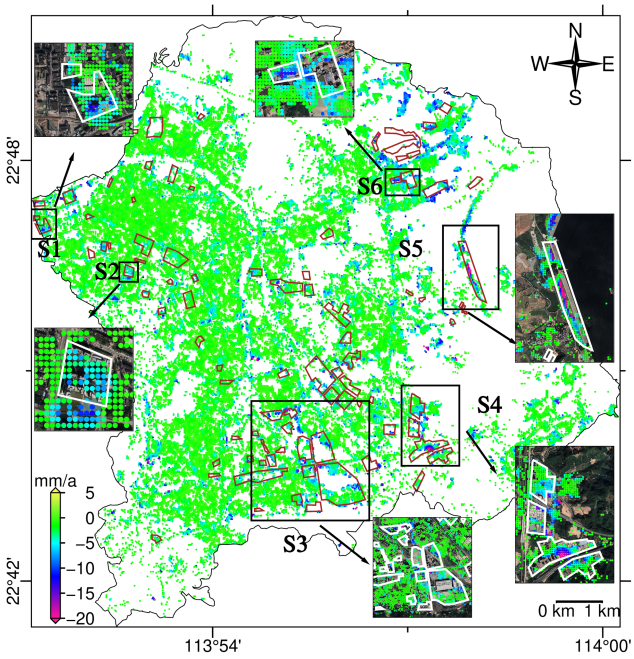

Fig. 15. Building changes between 2015 and 2021 in Guangming district of Shenzhen. The red polygons represent the building change areas. The background is the average deformation rate map. The black rectangles represent the selected areas with obvious subsidence.

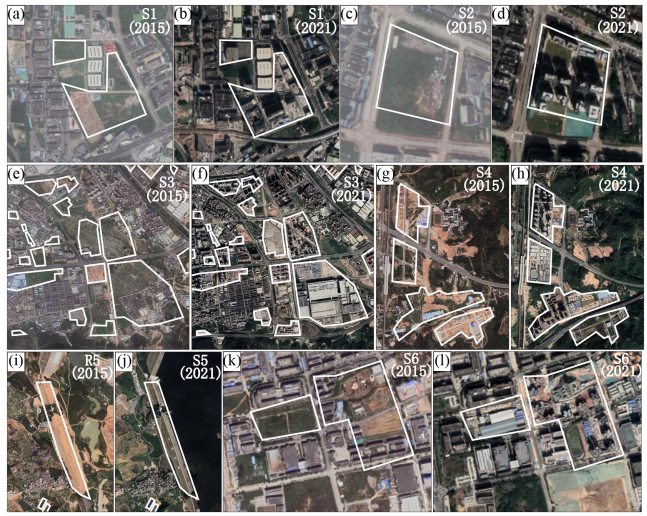

Fig. 16. Comparison of optical images between 2015 and 2021 for areas S1 to S6 in Fig. 13. The white polygons represent the building change areas.

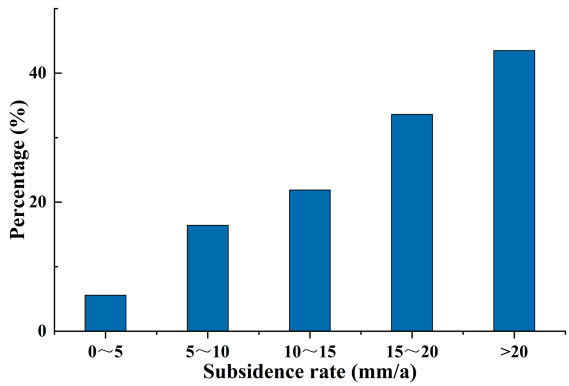

Fig. 17. Relationship between the subsidence rate and the building change percentage.

frequent human activities such as engineering construction can also accelerate land subsidence in the reclamation areas.

According to the previous analysis, land subsidence in the reclamation area of Shenzhen is mainly caused by the compaction of landfill material, underground exploitation, and ground infrastructure. Hence, three corresponding factors, distance from the coastline, distance from the subway, and road density, were selected to analyze the dominant factor that leads to land subsidence in reclamation areas. We used the Pearson correlation coefficient to calculate the correlation coefficient with a level of significance smaller than 0.1, as shown in Table III. The correlation coefficients are −0.101, −0.084, and −0.122 for the distance from the coastline, the distance from the subway, and road density, respectively. Among these three factors, the road density and the distance from the coastline showed a modest correlation with land subsidence.

E. Relationship Between Subsidence and Urban Construction in Guangming District

Guangming District is one of the most noticeable areas with urban expansion and urban construction in Shenzhen over the past few years. To analyze the relationship between land subsidence and urban construction, we adopted building change as a proxy for urban construction events in the Guangming district. We generated the newly added buildings between 2015 and 2021 with visual interpretation based on historical optical images, as shown in Fig. 15. The changing buildings are mainly located around the edge of the Guangming district, which is consistent with the trend of urban expansion. Additionally, land subsidence areas with obvious rates are mainly located within the changing areas. S1–S6 in Fig. 15 show the land subsidence within six typical regions of building change in the Guangming district. Fig. 16 shows a comparison of historical images of these regions during the six years. This indicates that urban construction may affect the occurrence of land subsidence.

In addition to the qualitative analysis, we also calculated the percentage of changing building areas. Specifically, we divided the subsidence rate into five grades and calculated the percentage of the changing building pixels of each grade. The histogram between these two factors is shown in Fig. 17. It is clear that the larger the subsidence rate grade is, the higher the percentage. The percentage for each grade is 5.57%, 16.4%, 21.88%, 33.59%, and 43.48%. Both qualitative and quantitative analyses prove that land subsidence in Guangming District has a high correlation with urban construction during the urbanization process.

F. Comparison With Other Studies

Many scholars have generated the deformation of Shenzhen in different periods based on SAR data [41], [43], [44], [45], as shown in Table IV. In these studies, subsidence areas were

TABLE IV
COMPARISON OF SUBSIDENCE PARAMETERS IN SHENZHEN WITH OTHER STUDIES

Authors	Datasets	Time span	Deformation velocity (mm/a)	Subsidence areas	Primary findings
Xu et al. [41]	Envisat ASAR	2007.2–2010.9	About −25 to 15 in the LOS direction	The reclamation areas: Shenzhen Airport, Baoan Center, Qianhai Bay, and Shenzhen Bay.	● Land subsidence occurred in land reclamation regions, especially in areas with reclamation before 2000. ● The ground deformation is expected to continue in the future.
He et al. [45]	Sentinel-1A (S1A), TerraSAR-X (TSX), LiDAR	S1A: 2017.3–2019.4 TSX: 2019.8–2020.5	About −40 to 12 in the vertical direction; About −22 to 20 in the vertical direction.	The reclamation areas: Houhai, Qianhai Bay, and the Wankeyuncheng. Position with maximum subsidence rate: near the Baoan Airport.	● The main causes of building subsidence are the construction of new buildings and underground activities.
Hu et al. [43]	Sentinel-1A	2016.1–2017.10	About −21.6 to 18.5 in the LOS direction.	The reclamation area: Qianhai District.	● The subsidence is more pronounced in areas with underground traffic facilities. ● Buildings with shallow foundations located in reclamation areas experienced significant subsidence.
Liu et al. [44]	Envisat ASAR, COSMO-SkyMed (CSK) Sentinel-1A	ASAR: 2006.9–2010.2 2004.11–2010.4 CSK: 2013.12–2016.1 S1A: 2015.6–2017.2	About −10 to 7 in the vertical direction.	Coastal areas: Qianhai, Houhai, south of Baoan International Airport, and subway.	● The subsidence is more pronounced in reclamation areas with subways. ● The seasonality of time series deformation is mainly related to precipitation.
This study	Sentinel-1A	2015.12–2021.7	About −74.9 to 5 in the LOS direction. Maximum subsidence rate of the local region: Baoan Airport: −66.2 Qianhai Bay: −38.2 Houhai: −44.3 Yantian Port: −22.1 Shajing community: −42	Coastal areas: Baoan International Airport, Qianhai Bay, Houhai, Yantian Port, and Guangming district. Along the subway: Line 11, Line 5. Position with maximum subsidence rate: near Shenzhen Convention and Exhibition Center.	● Land subsidence is mainly related to the typical urbanization process, such as land reclamation, urban construction, underground exploitation (subway), and road network density.

mainly distributed in the Qianhai bay, Houhai, and Baoan International Airport, with a maximum subsidence rate of 25 mm/a, 40 mm/a, and 21.6 mm/a for the period of 2007.2–2010.9, 2017.3–2019.4, 2016.1–2017.10, respectively. The causes of land subsidence mainly focused on land reclamation, underground activities, and building construction. Besides the spatial and temporal characteristics of subsidence, Xu et al. predicted that the subsidence along the coastal areas will continue after 2010 [41]. He et al. found that the safety of a building is affected by the construction phase difference and underground activities [45]. Liu et al. found that the seasonality of time series deformation in Shenzhen is mainly related to precipitation [44].

In this study, we generated the deformation of the entire Shenzhen except for a small area in the eastern. Areas with obvious subsidence are not only distributed on the coastal reclamation areas and along the subway, but also in the Shajing community and Yantian port with a maximum subsidence rate of 42 mm/a and 22.1 mm/a, respectively. The maximum subsidence rate of Baoan International airport, Qianhai bay, and Houhai reach 66.2 mm/a, 38.2 mm/a, and 44.3 mm/a respectively, which is larger than the value (25 mm/a) before 2010 [41]. This shows that the deformation of the three coastal areas is increasing from 2010 to 2021. In addition, we analyzed the relationship between land subsidence and typical urbanization process, such as land reclamation, urban construction, underground exploitation (subway), and road network density. The results show that land subsidence has a certain relationship with urban construction and road network density. Therefore, besides the reclamation areas, more attention should be paid to areas with intensive urban construction, low road density, and subway across in the future urbanization process, aiming to provide early warning for possible geological disasters.

V. CONCLUSION

In this study, we collected 153 Sentinel-1A images from 2015 to 2021 and adopted the IPTA-SBAS method to generate the time series deformation of Shenzhen. We qualitatively and quantitatively analyzed the spatial and temporal characteristics of land subsidence in Shenzhen. Land subsidence is mainly distributed along the coastal areas, especially in the Shajing community, Baoan International Airport, Qianhai Bay, Houhai, and Yantian Port. The maximum subsidence rate is approximately 74.9 mm/a. In addition to the coastal areas, obvious subsidence has also occurred in inland districts with abundant construction, such as the Guangming district. Land subsidence is mainly concentrated in the urban construction area, industrial area, farmed area, and residential area. Additionally, we also analyzed the subsidence along the 11 subways of Shenzhen. Among these metro lines, obvious subsidence has occurred along Line 11 and Line 5 with maximum subsidence rates of 71.5 mm/a and 53.4 mm/a, respectively.

Moreover, the relationship between land subsidence and typical urbanization progress was also discussed in the fields of land reclamation, transportation network including subway construction and road network density, and urban construction:

1) Land subsidence in the reclamation area is mainly caused by soft soil geological conditions and urban construction; 2) The correlation between the subsidence rate and the distance from the subway is weak, with a correlation coefficient of −0.197 when the subsidence rate was over 20 mm/a; 3) Land subsidence is more likely to occur in areas with low road network density; 4) Taking the Guangming district as an example, a positive correlation between land subsidence and urban construction is found, and obvious subsidence mainly occurs in areas with urban construction.

Based on the abovementioned conclusions, in addition to coastal areas of Shenzhen, more attention should be paid to inland areas with abundant urban constructions, low road density, and subway across for geological disaster monitoring in the future. The findings of this study can help guide urban planning and provide suggestions for government decision-making of similar cities.

ACKNOWLEDGMENT

The authors would like to thank the Associate Editor and anonymous reviewers for their constructive comments and suggestions that improved this paper greatly.

REFERENCES

[1] R. L. Hu, Z. Q. Yue, L. C. Wang, and S. J. Wang, "Review on current status and challenging issues of land subsidence in China," *Eng. Geol.*, vol. 76, no. 1, pp. 65–77, 2004.

[2] S. Dong, S. Samsonov, H. Yin, S. Ye, and Y. Cao, "Time-series analysis of subsidence associated with rapid urbanization in Shanghai, China measured with SBAS InSAR method," *Environ. Earth Sci.*, vol. 72, no. 3, pp. 677–691, 2014.

[3] A. Kulshrestha, L. Chang, and A. Stein, "Use of LSTM for sinkhole-related anomaly detection and classification of InSAR deformation time series," *IEEE J. Sel. Topics Appl. Earth Observ. Remote Sens.*, vol. 15, pp. 4559–4570, 2022.

[4] J. Catalao, D. Raju, and G. Nico, "Insar maps of land subsidence and sea level scenarios to quantify the flood inundation risk in coastal cities: The case of Singapore," *Remote Sens.*, vol. 12, no. 2, 2020, Art. no. 296.

[5] X. Diao, K. Wu, R. Chen, and J. Yang, "Identifying the cause of abnormal building damage in mining subsidence areas using InSAR technology," *IEEE Access*, vol. 7, pp. 172296–172304, 2019.

[6] W. Tang, W. Zhan, B. Jin, M. Motagh, and Y. Xu, "Spatial variability of relative sea-level rise in Tianjin, China: Insight from InSAR, GPS, and tide-gauge observations," *IEEE J. Sel. Topics Appl. Earth Observ. Remote Sens.*, vol. 14, pp. 2621–2633, 2021.

[7] Y. Du, G. Feng, L. Liu, H. Fu, X. Peng, and D. Wen, "Understanding land subsidence along the coastal areas of Guangdong, China, by analyzing multi-track MTInSAR data," *Remote Sens.*, vol. 12, no. 2, 2020, Art. no. 299.

[8] L. Yi et al., "Impacts of human activities on coastal ecological environment during the rapid urbanization process in Shenzhen, China," *Ocean Coastal Manage.*, vol. 154, pp. 121–132, 2018.

[9] Z. Gao, X. He, R. Xiao, J. Yu, and H. Luo, "Development of an imagewise stacking method to mitigate atmospheric effect with an application to Lianyan Railway," *IEEE J. Sel. Topics Appl. Earth Observ. Remote Sens.*, vol. 14, pp. 4787–4797, 2021.

[10] S. Wu, Z. Yang, X. Ding, B. Zhang, L. Zhang, and Z. Lu, "Two decades of settlement of Hong Kong international airport measured with multi-temporal InSAR," *Remote Sens. Environ.*, vol. 248, 2020, Art. no. 111976.

[11] Z. Du, L. Ge, A. H.-M. Ng, Q. Zhu, F. G. Horgan, and Q. Zhang, "Risk assessment for tailings dams in Brumadinho of Brazil using InSAR time series approach," *Sci. Total Environ.*, vol. 717, 2020, Art. no. 137125.

[12] M. Jiang and A. M. Guarnieri, "Distributed scatterer interferometry with the refinement of spatiotemporal coherence," *IEEE Trans. Geosci. Remote Sens.*, vol. 58, no. 6, pp. 3977–3987, Jun. 2020.

[13] C. Huang, H. Xia, and J. Hu, "Surface deformation monitoring in coal mine area based on PSI," *IEEE Access*, vol. 7, pp. 29672–29678, 2019.

[14] Y. Chen, Y. Tong, and K. Tan, "Coal mining deformation monitoring using SBAS-InSAR and offset tracking: A case study of Yu County, China," *IEEE J. Sel. Topics Appl. Earth Observ. Remote Sens.*, vol. 13, pp. 6077–6087, 2020.

[15] Y. Kang, Z. Lu, C. Zhao, Y. Xu, J.-W. Kim, and A. J. Gallegos, "InSAR monitoring of creeping landslides in mountainous regions: A case study in Eldorado National Forest, California," *Remote Sens. Environ.*, vol. 258, 2021, Art. no. 112400.

[16] K. Dai et al., "Entering the era of Earth observation-based landslide warning systems: A novel and exciting framework," *IEEE Geosci. Remote Sens. Mag.*, vol. 8, no. 1, pp. 136–153, Mar. 2020.

[17] E. Chaussard, F. Amelung, H. Abidin, and S.-H. Hong, "Sinking cities in Indonesia: ALOS PALSAR detects rapid subsidence due to groundwater and gas extraction," *Remote Sens. Environ.*, vol. 128, pp. 150–161, 2013.

[18] E. Chaussard, S. Wdowinski, E. Cabral-Cano, and F. Amelung, "Land subsidence in central Mexico detected by ALOS InSAR time-series," *Remote Sens. Environ.*, vol. 140, pp. 94–106, 2014.

[19] Y. Du, H. Fu, L. Liu, G. Feng, X. Peng, and D. Wen, "Orbit error removal in InSAR/MTInSAR with a patch-based polynomial model," *Int. J. Appl. Earth Observ. Geoinf.*, vol. 102, 2021, Art. no. 102438.

[20] D. Suresh and K. Yarrakula, "InSAR based deformation mapping of earthquake using Sentinel 1A imagery," *Geocarto Int.*, vol. 35, no. 5, pp. 559–568, 2020.

[21] J. R. Elliott, R. J. Walters, and T. J. Wright, "The role of space-based observation in understanding and responding to active tectonics and earthquakes," *Nature Commun.*, vol. 7, no. 1, 2016, Art. no. 13844.

[22] E. Chaussard and F. Amelung, "Precursory inflation of shallow magma reservoirs at west Sunda volcanoes detected by InSAR," *Geophys. Res. Lett.*, vol. 39, 2012, Art. no. 21.

[23] A. Hooper, H. Zebker, P. Segall, and B. Kampes, "A new method for measuring deformation on volcanoes and other natural terrains using InSAR persistent scatterers," *Geophys. Res. Lett.*, vol. 31, 2004, Art. no. 23.

[24] A. Hooper, P. Segall, and H. Zebker, "Persistent scatterer interferometric synthetic aperture radar for crustal deformation analysis, with application to Volcán Alcedo, Galápagos," *J. Geophys. Res.*, vol. 112, 2007, Art. no. B7.

[25] C. Zhou et al., "Application of an improved multi-temporal InSAR method and forward geophysical model to document subsidence and rebound of the Chinese Loess Plateau following land reclamation in the Yan'an New District," *Remote Sens. Environ.*, vol. 279, 2022, Art. no. 113102.

[26] M. Liao et al., "Subsidence monitoring of fill area in Yan'an new district based on sentinel-1A time series imagery," *Remote Sens.*, vol. 13, no. 15, 2021, Art. no. 3044.

[27] Q. Wu, C. Jia, S. Chen, and H. Li, "SBAS-InSAR based deformation detection of urban land, created from mega-scale mountain excavating and valley filling in the loess plateau: The case study of Yan'an City," *Remote Sens.*, vol. 11, no. 14, 2019, Art. no. 1673.

[28] X. Hu et al., "Remote sensing characterization of mountain excavation and City construction in Loess Plateau," *Geophys. Res. Lett.*, vol. 48, no. 21, 2021, Art. no. e2021GL095230..

[29] F. Cigna and D. Tapete, "Urban growth and land subsidence: Multi-decadal investigation using human settlement data and satellite InSAR in Morelia, Mexico," *Sci. Total Environ.*, vol. 811, 2022, Art. no. 152211.

[30] C. E. Duffy, A. Braun, and V. Hochschild, "Surface subsidence in urbanized coastal areas: PSI methods based on Sentinel-1 for Ho Chi Minh City," *Remote Sens.*, vol. 12, no. 24, 2020, Art. no. 2130.

[31] G. Chen et al., "Detection of land subsidence associated with land creation and rapid urbanization in the Chinese loess plateau using time series InSAR: A case study of Lanzhou new district," *Remote Sens.,* vol. 10, no. 2, 2018, Art. no. 270.

[32] Y. He, Y. Chen, W. Wang, H. Yan, L. Zhang, and T. Liu, "TS-InSAR analysis for monitoring ground deformation in Lanzhou New District, the loess Plateau of China, from 2017 to 2019," *Adv. Space Res.*, vol. 67, no. 4, pp. 1267–1283, 2021.

[33] B. B. Chen et al., "Spatial correlation between land subsidence and urbanization in Beijing, China," *Natural Hazards.*, vol. 75, no. 3, pp. 2637–2652, 2015.

[34] C. Zhou et al., "Quantifying the contribution of multiple factors to land subsidence in the Beijing Plain, China with machine learning technology," *Geomorphology*, vol. 335, pp. 48–61, 2019.

[35] M. Motagh et al., "Quantifying groundwater exploitation induced subsidence in the Rafsanjan plain, southeastern Iran, using InSAR time-series and in situ measurements," *Eng. Geol.*, vol. 218, pp. 134–151, 2017.

[36] Y. Han, J. Zou, Z. Lu, F. Qu, Y. Kang, and J. Li, "Ground deformation of Wuhan, China, revealed by multi-temporal InSAR analysis," *Remote Sens.,* vol. 12, no. 22, 2020, Art. no. 3788.
[37] L. Guo et al., "Understanding uneven land subsidence in Beijing, China, using a novel combination of geophysical prospecting and InSAR," *Geophys. Res. Lett.*, vol. 47, no. 16, 2020, Art. no. e2020GL088676.
[38] B. Hu and Z. Li, "Time-series InSAR technology for ascending and descending orbital images to monitor surface deformation of the metro network in Chengdu," *IEEE J. Sel. Topics Appl. Earth Observ. Remote Sens.*, vol. 14, pp. 12583–12597, 2021.
[39] L. Solari, A. Ciampalini, F. Raspini, S. Bianchini, and S. Moretti, "PSInSAR analysis in the Pisa urban area (Italy): A case study of subsidence related to stratigraphical factors and urbanization," *Remote Sens.*, vol. 8, no. 2, 2016, Art no. 120.
[40] Q. Yang et al., "Multi-scale analysis of the relationship between land subsidence and buildings: A case study in an eastern Beijing urban area using the PS-InSAR technique," *Remote Sens.*, vol. 10, no. 7, 2018, Art no. 1006.
[41] B. Xu, G. C. Feng, Z. W. Li, Q. J. Wang, C. C. Wang, and R. G. Xie, "Coastal subsidence monitoring associated with land reclamation using the point target based SBAS-InSAR method: A case study of Shenzhen, China," *Remote Sens.*, vol. 8, no. 8, 2016, Art no. 652.
[42] H. Wang et al., "InSAR reveals coastal subsidence in the Pearl River Delta, China," *Geophysical J. Int.*, vol. 191, no. 3, pp. 1119–1128, 2012.
[43] B. Hu, J. Y. Chen, and X. F. Zhang, "Monitoring the land subsidence area in a coastal urban area with InSAR and GNSS," *Sensors,* vol. 19, no. 14, 2019, Art no. 3181.
[44] P. Liu et al., "Resolving surface displacements in Shenzhen of China from time series InSAR," *Remote Sens.*, vol. 10, no. 7, 2018, Art no. 1162.
[45] Y. F. He, G. C. Xu, H. Kaufmann, J. T. Wang, H. Ma, and T. Liu, "Integration of InSAR and LiDAR technologies for a detailed urban subsidence and hazard assessment in Shenzhen, China," *Remote Sens.*, vol. 13, no. 12, 2021, Art no. 2366.
[46] C. Xu, H.-H. Wang, Z.-C. Luo, J.-S. Ning, and H.-L. Liu, "Multilayer stress from gravity and its tectonic implications in urban active fault zone: A case study in Shenzhen, South China," *J. Appl. Geophys.*, vol. 114, pp. 174–182, 2015.
[47] L. Zhou et al., "Monitoring of land subsidence in Shenzhen reclamation area based on Sentinel-1A interferometric synthetic aperture radar," *Sci. Technol. Eng.*, vol. 21, pp. 8765–8769, Jul. 2021.
[48] P. Berardino, G. Fornaro, R. Lanari, and E. Sansosti, "A new algorithm for surface deformation monitoring based on small baseline differential SAR interferograms," *IEEE Trans. Geosci. Remote Sens.*, vol. 40, no. 11, pp. 2375–2383, Nov. 2002.
[49] A. Ferretti, C. Prati, and F. Rocca, "Permanent scatterers in SAR interferometry," *IEEE Trans. Geosci. Remote Sens.*, vol. 39, no. 1, pp. 8–20, Jan. 2001.
[50] A. K. Gabriel, R. M. Goldstein, and H. A. Zebker, "Mapping small elevation changes over large areas: Differential radar interferometry," *J. Geophysical Res., Solid Earth*, vol. 94, no. B7, pp. 9183–9191, 1989.
[51] C. Werner, U. Wegmuller, T. Strozzi, and A. Wiesmann, "Interferometric point target analysis for deformation mapping," in *Proc . IEEE Int. Geosci. Remote Sens. Symp.*, 2003, vol. 7, pp. 4362–4364.
[52] A. Ferretti, C. Prati, and F. Rocca, "Nonlinear subsidence rate estimation using permanent scatterers in differential SAR interferometry," *IEEE Trans. Geosci. Remote Sens.*, vol. 38, no. 5, pp. 2202–2212, Sep. 2000.
[53] G. Blewitt, W. C. Hammond, and C. Kreemer, "Harnessing the GPS data explosion for interdisciplinary science," *EOS*, vol. 99, no. 10.1029, 2018, Art. no. 485.
[54] W. C. Hammond and J. W. Bell, "Structural controls on geothermal reservoir deformation at Stillwater, Nevada from InSAR and GPS data," *GRC Trans.*, vol. 37, pp. 11–15, 2013.
[55] J. Overacker et al., "Vertical land motion of the High Plains Aquifer region of the United States: Effect of aquifer confinement style, climate variability, and anthropogenic activity," *Water Resour Res.*, vol. 58, no. 6, 2022, Art. no. e2021WR031635.
[56] J. Xu, M. Jiang, V. G. Ferreira, and Z. Wu, "Time-series InSAR dynamic analysis with robust sequential adjustment," *IEEE Geosci. Remote Sens. Lett.*, vol. 19, 2022, Art. no. 4514405.
[57] R. A. Ramirez et al., "Monitoring of construction-induced urban ground deformations using Sentinel-1 PS-InSAR: The case study of tunneling in Dangjin, Korea," *Int. J. Appl. Earth Observ. Geoinf.*, vol. 108, Jan. 2022, Art. no. 102721.
[58] A. H. Ng et al., "InSAR reveals land deformation at Guangzhou and Foshan, China between 2011 and 2017 with COSMO-SkyMed Data," *Remote Sens.*, vol. 10, no. 6, 2018, Art. no. 813.
[59] H. Guo et al., "Groundwater-derived land subsidence in the North China plain," *Environ. Earth Sci.*, vol. 74, no. 2, pp. 1415–1427. 2015.
[60] H. Akoglu, "User's guide to correlation coefficients," *Turkish J. Emerg. Med.*, vol. 18, no. 3, pp. 91–93, 2018.
[61] J. Li et al., "Surface deformation mechanism analysis in Shanghai areas based on TS-InSAR technology," *Remote Sens.*, vol. 14, no. 17, 2022, Art. no. 4368.

Min Sun received the B.S. degree in surveying and mapping engineering from Central South University, Changsha, China, in 2020. He is currently working toward the M.S. degree in surveying and mapping engineering with the School of Geography and Remote Sensing, Guangzhou University, Guangzhou, China.

His major research interests include interferometric synthetic aperture radar for ground deformation monitoring and early warning of geological disaster.

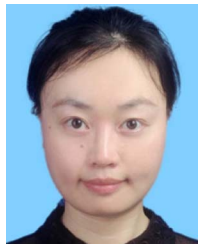

Yanan Du received the B.S. and Ph.D. degrees in geodesy and surveying engineering from the School of Geosciences and Info-Physics, Central South University, Changsha, China, in 2011 and 2017, respectively.

She is currently an Associate Professor with the School of Geography and Remote Sensing, Guangzhou University, Guangzhou, China. Her current research interests include interferometric synthetic aperture radar and its applications on digital elevation model reconstruction and surface deformation mapping.

Qingyao Liu received the B.S. degree in surveying and mapping engineering from Central South University, Changsha, China, in 2020. She is currently working toward the M.S. degree in surveying and mapping engineering with the School of Geography and Remote Sensing, Guangzhou University, Guangzhou, China.

Her major research interests include interferometric synthetic aperture radar for landslide monitoring and parameter inversion.

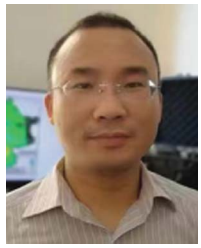

Guangcai Feng received the master's degree in surveying engineering from Central South University, Changsha, China, in 2006, and the Ph.D. degree in geophysics and geodesy from the Hong Kong Polytechnic University, Hong Kong, in 2011.

He is currently a Full Professor with the Department of Surveying and Remote Sensing, School of Geoscience and Info-Physics, Central South University, Changsha, China. His research interests include interferometric synthetic aperture radar for inverting source parameters of earthquakes and ground deformation monitoring in urban areas.

Xing Peng received the M.S. degree in geodesy from the Central South University, Changsha, China, in 2011, and the Ph.D. degree in photogrammetry and remote sensing from the Central South University, Changsha, China, in 2018.

She received the funding from the China Scholarship Council for a one-year joint Ph.D. training at the Laboratory of Electronic Communication (IETR), University of Rennes 1, France, from 2015 to 2016. She is currently working an Associate Professor and master's supervisor of the School of Geography and Information Engineering, China University of Geosciences (Wuhan). Her research interests include high-resolution SAR tomography 3-D imaging algorithms and their applications in urban, forest and glaciers, such as urban topography mapping, forest underlying topography estimation and forest height inversion, forest biomass estimation, etc.

Chunhua Liao is currently working toward the B.S. degree in geographic information system with the School of Geography and Remote Sensing, Guangzhou University, Guangzhou, China.

Her major research is interferometric synthetic aperture radar and its application on deformation monitoring of subway line.